Volume 53
Number 26
14 July 2024
Pages 10757-11178

Dalton Transactions

An international journal of inorganic chemistry

rsc.li/dalton

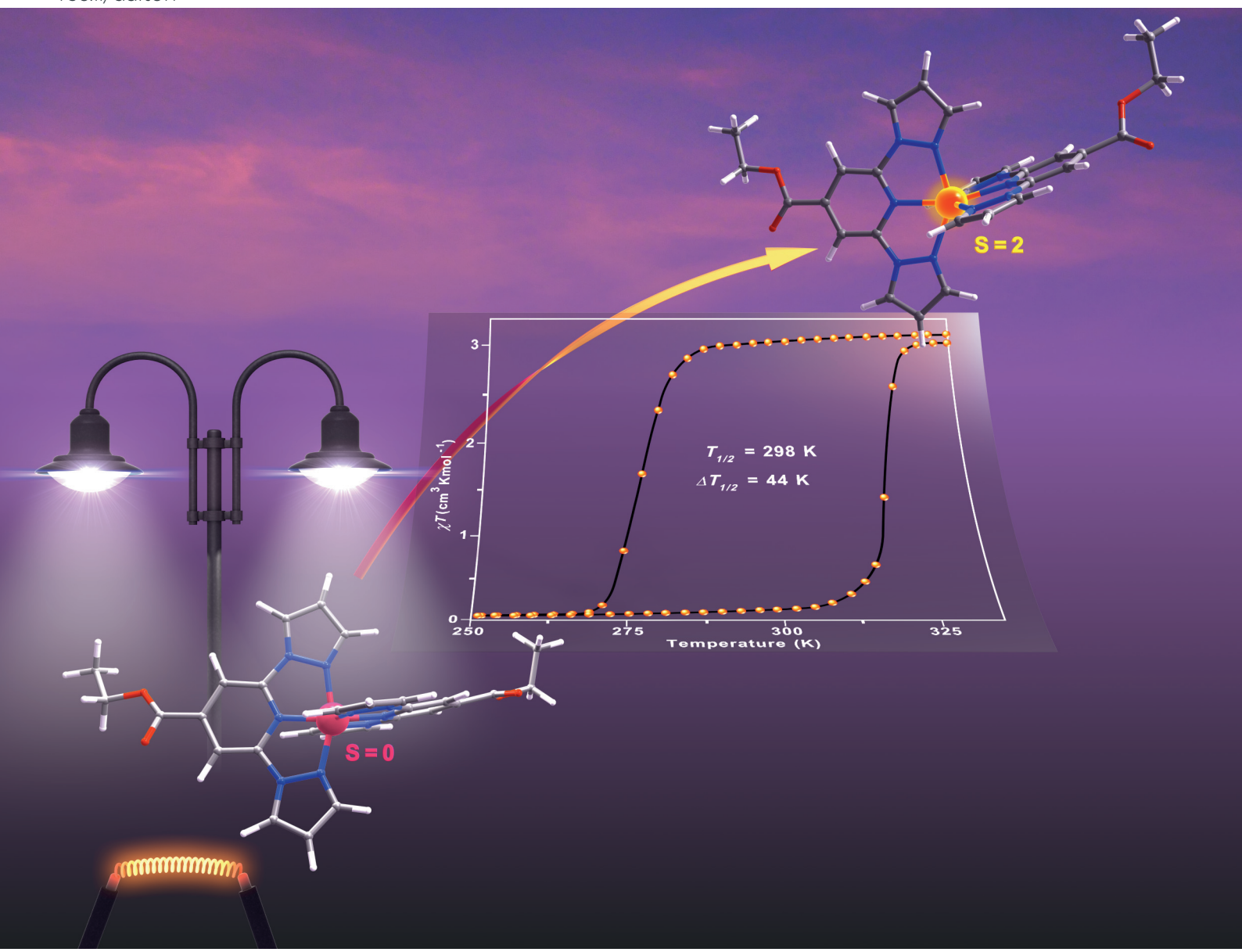

ISSN 1477-9226

ROYAL SOCIETY OF CHEMISTRY

PAPER

Senthil Kumar Kuppusamy *et al.*

Lattice solvent- and substituent-dependent spin-crossover in isomeric iron(II) complexes

Dalton Transactions

ROYAL SOCIETY OF CHEMISTRY

PAPER

View Article Online
View Journal | View Issue

Check for updates

Cite this: *Dalton Trans.*, 2024, **53**, 10851

Lattice solvent- and substituent-dependent spin-crossover in isomeric iron(II) complexes†

Senthil Kumar Kuppusamy, *[a] Asato Mizuno,‡[b] Lea Kämmerer, [c] Soma Salamon, [c] Benoît Heinrich, [d] Corinne Bailly,[e] Ivan Šalitroš, *[f,g] Heiko Wende *[c] and Mario Ruben*[a,b,h]

Spin-state switching in iron(II) complexes composed of ligands featuring moderate ligand-field strength—for example, 2,6-bi(1*H*-pyrazol-1-yl)pyridine (BPP)—is dependent on many factors. Herein, we show that spin-state switching in isomeric iron(II) complexes composed of BPP-based ligands—ethyl 2,6-bis(1*H*-pyrazol-1-yl)isonicotinate (BPP-COOEt, **L1**) and (2,6-di(1*H*-pyrazol-1-yl)pyridin-4-yl)methylacetate (BPP-CH_2OCOMe, **L2**)—is dependent on the nature of the substituent at the BPP skeleton. Bi-stable spin-state switching—with a thermal hysteresis width ($\Delta T_{1/2}$) of 44 K and switching temperature ($T_{1/2}$) = 298 K in the first cycle—is observed for complex **1**·CH_3CN composed of **L1** and BF_4^- counter anions. Conversely, the solvent-free isomeric counterpart of **1**·CH_3CN—complex **2a**, composed of **L2** and BF_4^- counter anions—was trapped in the high-spin (HS) state. For one of the polymorphs of complex **2b**·CH_3CN—**2b**·CH_3CN-Y, Y denotes yellow colour of the crystals—composed of **L2** and ClO_4^- counter anions, a gradual and non-hysteretic SCO is observed with $T_{1/2}$ = 234 K. Complexes **1**·CH_3CN and **2b**·CH_3CN-Y also underwent light-induced spin-state switching at 5 K due to the light-induced excited spin-state trapping (LIESST) effect. Structures of the low-spin (LS) and HS forms of complex **1**·CH_3CN revealed that spin-state switching goes hand-in-hand with pronounced distortion of the *trans*-*N*{pyridyl}-Fe–N{pyridyl} angle (ϕ), whereas such distortion is not observed for **2b**·CH_3CN-Y. This observation points that distortion is one of the factors making the spin-state switching of **1**·CH_3CN hysteretic in the solid state. The observation of bi-stable spin-state switching with $T_{1/2}$ centred at room temperature for **1**·CH_3CN indicates that technologically relevant spin-state switching profiles based on mononuclear iron(II) complexes can be obtained.

Received 14th February 2024,
Accepted 15th May 2024

DOI: 10.1039/d4dt00429a

rsc.li/dalton

Open Access Article. Published on 22 May 2024. Downloaded on 9/16/2024 9:40:39 PM.
This article is licensed under a Creative Commons Attribution 3.0 Unported Licence.

Introduction

Molecular materials that show switching of a physical property—for example, magnetic[1–12] or electric[13–17]—accompanied by hysteresis are candidates desirable for applications. Several classes of magnetic-molecular systems such as organic radicals,[18–20] single-molecule magnets (SMMs),[3,21–23] and spin-crossover (SCO) complexes[24–31] are known to show bistable switching characteristics. However, to the best of our knowledge, SCO complexes are the only class of molecules that frequently show bistable switching near room-temperature (RT).[4,12] For realistic applications, SCO complexes showing a

[a]*Institute of Quantum Materials and Technologies (IQMT), Karlsruhe Institute of Technology (KIT), Hermann-von-Helmholtz-Platz 1, 76344 Eggenstein-Leopoldshafen, Germany. E-mail: senthil.kuppusamy2@kit.edu*
[b]*Institute of Nanotechnology (INT), Karlsruhe Institute of Technology (KIT), Hermann-von-Helmholtz-Platz 1, 76344 Eggenstein-Leopoldshafen, Germany*
[c]*University of Duisburg-Essen, Faculty of Physics and Center for Nanointegration Duisburg-Essen (CENIDE), Lotharstraße 1, 47057 Duisburg, Germany*
[d]*Institut de Physique et Chimie des Matériaux de Strasbourg (IPCMS), CNRS-Université de Strasbourg, 23, rue du Loess, BP 43, 67034 Strasbourg Cedex 2, France*
[e]*Service de Radiocristallographie, Fédération de Chimie Le Bel UAR2042 CNRS-Université de Strasbourg, 1 rue Blaise Pascal, BP 296/R8, 67008 Strasbourg cedex, France*
[f]*Central European Institute of Technology, Brno University of Technology, Purkyňova 123, 61200 Brno, Czech Republic*
[g]*Department of Inorganic Chemistry, Faculty of Chemical and Food Technology, Slovak University of Technology in Bratislava, Bratislava SK-81237, Slovakia*
[h]*Centre Européen de Sciences Quantiques (CESQ), Institut de Science et d'Ingénierie, Supramoléculaires (ISIS), 8 allée Gaspard Monge, BP 70028, 67083 Strasbourg Cedex, France*

† Electronic supplementary information (ESI) available. CCDC 1560719, 1913041, 1953349, 1953350, 1988543, 2330938, 2330939 and 2340087. For ESI and crystallographic data in CIF or other electronic format see DOI: https://doi.org/10.1039/d4dt00429a

‡ Current address: Department of Materials Engineering Science, Graduate School of Engineering Science, Osaka University, 1-3 Machikaneyama, Toyonaka, Osaka 560-8531, Japan.

Open Access Article. Published on 22 May 2024. Downloaded on 9/16/2024 9:40:39 PM.
This article is licensed under a Creative Commons Attribution 3.0 Unported Licence.

sizable thermal hysteresis width ($\Delta T_{1/2}$)—around 70 K—with the switching temperature ($T_{1/2}$) centred around RT are desirable.[4] However, preparing an SCO complex that can undergo hysteretic switching around RT is not a trivial task because spin-state switching in the solid state is controlled by system-dependent factors, such as lattice solvent and disorder. Therefore, it is necessary to conduct a systematic search starting from a basic ligand skeleton featuring a moderate ligand field allowing spin-state switching of a coordinated metal ion, iron(II) in the context of this study. 2,6-Bis(1*H*-pyrazol-1-yl)pyridine (BPP)-based ligands (Fig. 1a) are a class of tridentate nitrogen-donor ligands that facilitate spin-state switching of the coordinated iron(II) centre, as first reported by Halcrow and co-workers in 2001.[32] The propensity to modify the BPP skeleton with functional groups at the pyridine and pyrazole rings allows the systematic study of spin-state switching of the iron(II)–BPP complexes, useful for establishing structure–SCO property correlations.[33] Recently, technologically relevant spin-state switching characteristics of iron(II) complexes (complexes **a**–**d**, Fig. 1b) composed of a BPP-based ligand—ethyl 2,6-bis(1*H*-pyrazol-1-yl)isonicotinate (BPP-COOEt, **L1**)—have been reported. Complex **a** underwent above room-temperature low-spin (LS)-to-high-spin (HS) switching and remained trapped in the HS-state after the loss of lattice acetone solvent.[34] On the other hand, complex **b**, co-crystallized with lattice acetonitrile, underwent bi-stable spin-state switching with $T_{1/2}$ = 233 K and $\Delta T_{1/2}$ = 100 K in the first cycle.[9] However, in the subsequent cycles spin-state switching of complex **b** is rendered unstable due to self-grinding of the crystals. In a subsequent report, some of us have reported on the stable spin-state switching characteristics of complexes **c** and **d** and elucidated on the role of pronounced molecular distortion as a factor contributing to the occurrence of hysteretic spin-state switching.[35] In this contribution, we have studied iron(II) complexes composed of BPP-COOEt (**L1**) and (2,6-di(1*H*-pyrazol-1-yl)pyridin-4-yl) methylacetate (BPP-CH_2OCOMe, **L2**) ligands (Fig. 1a). Complex **1**·CH_3CN (Fig. 1b), composed of the BPP-COOEt ligand and BF_4^- counter anions, undergoes bi-stable spin-state switching ($\Delta T_{1/2}$ = 44 K) with $T_{1/2}$ centred at RT (298 K) in the first cycle and the switching is not stable upon repeated cycling. To study the impact of substituents on the switching characteristics, we have prepared a new ligand **L2**, which features the same molecular formula as **L1**—the ligands **L1** and **L2** are structural isomers. Complex **2a** (Fig. 1c) composed of **L2** crystallized without the lattice solvent and showed no spin-state switching from the HS state upon cooling from 300 K. Conversely, for complex **2b**·CH_3CN-Y (Fig. 1c), a gradual SCO without thermal hysteresis is observed. Remarkably, complexes

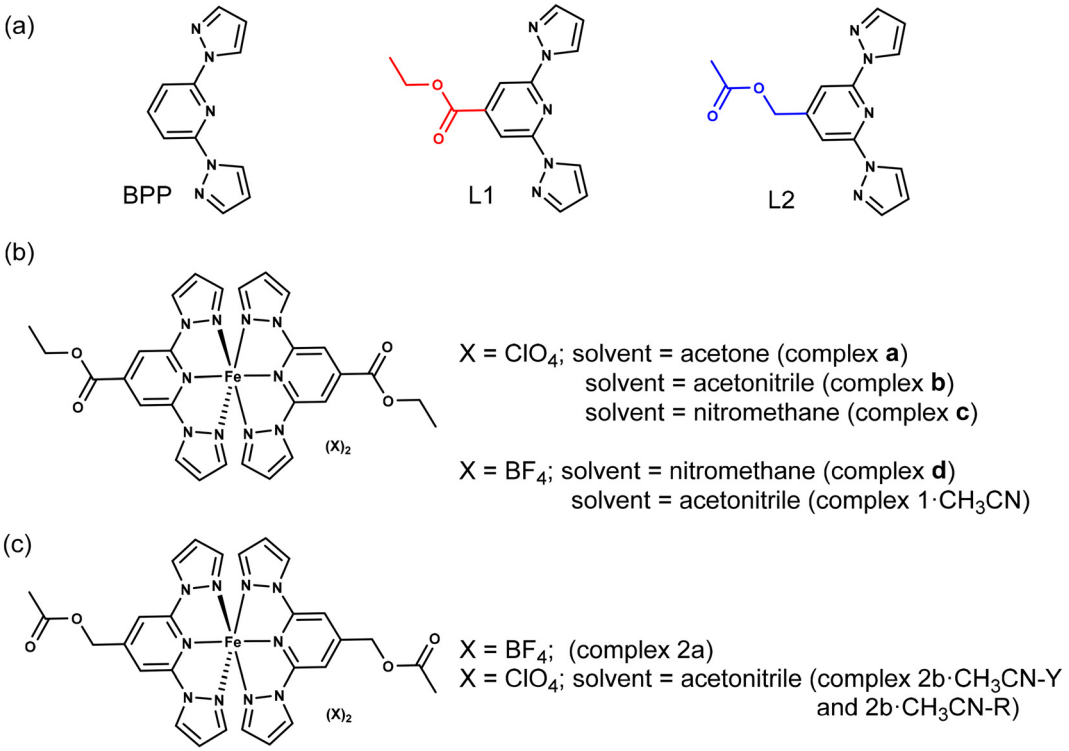

Fig. 1 Molecular structures of ligands and iron(II) complexes discussed in this study. (a) Structures of parent BPP ligand and its functional variants **L1** and **L2**. The ligands **L1** and **L2** are structural isomers; red and blue colours highlight functional group isomerism. The aim of this study is to elucidate how the nature of the substituent controls spin-state switching in iron(II) complexes composed of **L1** and **L2**. (b) Structures of **L1**-based complexes **a**, **b**, **c**, **d**, and **1**·CH_3CN. (c) Structures of **L2**-based complexes **2a** and **2b**·CH_3CN. For **2b**·CH_3CN, two different polymorphs—**2b**·CH_3CN-Y and **2b**·CH_3CN-R—were obtained; Y and R denote yellow and red, respectively, colours of the crystals. Iron(II) complexes **a**, **b**, **c**, and **d** have been studied previously.[9,34,35]

 This journal is © The Royal Society of Chemistry 2024

Open Access Article. Published on 22 May 2024. Downloaded on 9/16/2024 9:40:39 PM. This article is licensed under a Creative Commons Attribution 3.0 Unported Licence.

1·CH_3CN and **2b**·CH_3CN-Y also underwent light-induced LS-to-HS switching at 5 K following the light-induced excited spin-state trapping (LIESST) mechanism. The molecular structures of the LS and HS forms of **1**·CH_3CN obtained from single-crystal X-ray diffraction (SC-XRD) studies revealed a pronounced angular distortion of the *trans-N*{pyridyl}-Fe–N{pyridyl} angle (ϕ) in the HS-form relative to the LS-form. Additionally, the conformation of the ethyl substituent of **1**·CH_3CN is also switched upon spin-state switching. In contrast, no significant variation of ϕ was observed for the LS and HS forms of **2b**·CH_3CN-Y. These results indicate the contributory role of molecular distortion in spurring the bi-stable spin-state switching observed for **1**·CH_3CN. Overall, the contrasting magnetic characteristics of the complexes show a complex interplay between structural- and spin-isomerism, and a structural control over SCO is achievable following molecular engineering principles. Crucially, complex **1**·CH_3CN is one of the remarkable examples of a mononuclear iron(II) complex that undergoes temperature-induced bistable SCO with a $T_{1/2}$ centred at RT. Importantly, our attribution that pronounced molecular distortion and a change in substituent conformation contribute to the opening of the thermal hysteresis loop could enable future designs of iron(II)-based SCO complexes with application-oriented spin-state switching characteristics.

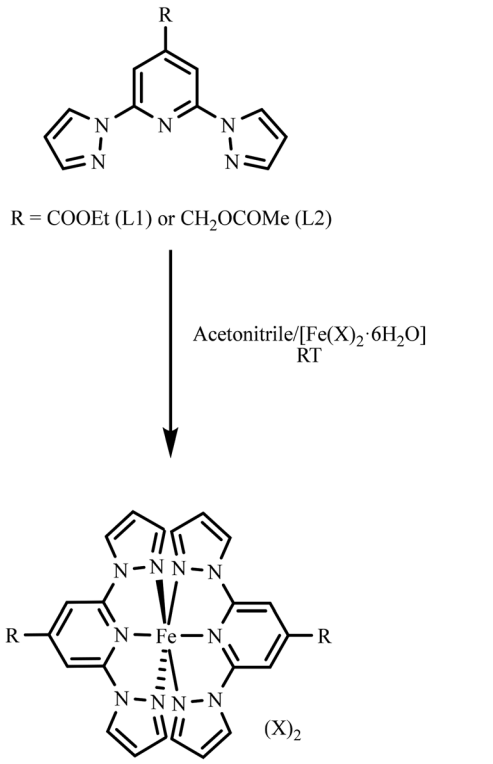

R = COOEt, X = BF_4 (1·CH_3CN)
R = CH_2OCOMe, X = BF_4 (2a)
R = CH_2OCOMe, X = ClO_4 (2b·CH_3CN-Y and 2b·CH_3CN-R)

Scheme 1 Preparation of complex **1**·CH_3CN from **L1** and complexes **2a** and **2b**·CH_3CN from **L2**. Two different polymorphs coloured yellow (**2b**·CH_3CN-Y) and red (**2b**·CH_3CN-R) were obtained for **2b**·CH_3CN.

Experimental

Materials and methods

Anhydrous solvents, $[Fe(BF_4)_2{\cdot}6H_2O]$, and $[Fe(ClO_4)_2{\cdot}6H_2O]$ were purchased from commercial sources and used as received. Glassware was dried in a vacuum oven at 423 K prior to the experiments. The complexation reactions were performed under an argon (Ar) atmosphere. Experimental protocols used to study the physical properties of the ligands and complexes (section S1), and synthesis procedures used to prepare the ligands and complexes (section S2) are described in the ESI.†

Caution: perchlorate salts are potentially hazardous; care should be taken while handling them. We have encountered no difficulties during the preparation, characterization, and magnetic studies of perchlorate containing complexes—**2b**·CH_3CN-Y and **2b**·CH_3CN-R—discussed in this study.

Results and discussion

Synthesis of the ligands and complexes

Ligand **L1** was synthesized following a previously reported procedure.[36] Ligand **L2** was synthesized from (2,6-di(1*H*-pyrazol-1-yl)pyridin-4-yl)methanol, as detailed in section S2 of the ESI.† Treatment of $[Fe(X)_2{\cdot}6H_2O]$ (X = BF_4 or ClO_4) as a solid with the acetonitrile solution of the respective ligand resulted in the formation of complexes **1**·CH_3CN, **2a**, or **2b**·CH_3CN (Scheme 1). Slow diffusion of diethyl ether into the acetonitrile solutions of the reaction mixtures kept inside a fridge at 4 °C over a period of 2–3 weeks yielded a crop of wine-red crystals of complex **1**·CH_3CN and pale-yellow crystals of **2a**, suitable for single-crystal X-ray diffraction (SC-XRD) studies. In the case of **2b**·CH_3CN, crystallizing with lattice acetonitrile, two different polymorphs coloured yellow (**2b**·CH_3CN-Y) and red (**2b**·CH_3CN-R) were obtained. After harvesting from the mother liquor, the crystals of **1**·CH_3CN were washed with diethyl ether and dried under vacuum for 4 h. Elemental analysis of the dried crystals revealed that lattice acetonitrile solvent is retained after the drying process (section S2†). In the case of **2b**·CH_3CN-Y, drying under vacuum resulted in the loss of the lattice solvent. Therefore, the yellow crystals were left to dry inside a fume-hood for an hour after washing with diethyl ether. We have also noted slow release of the lattice solvent from the crystals of **2b**·CH_3CN-Y over the course of a few days while storing under ambient conditions. The crystals of **2b**·CH_3CN-R lost the lattice solvent rapidly after removing from the mother liquor with the consequent cracking and yellow-brown coloration of the crystals. A complete loss of the lattice solvent was inferred from the elemental analysis data of **2b**·CH_3CN-R. See section S2 and Fig. S1–S6 of the ESI† for the characterization data of the ligands and complexes.

Open Access Article. Published on 22 May 2024. Downloaded on 9/16/2024 9:40:39 PM.
This article is licensed under a Creative Commons Attribution 3.0 Unported Licence.

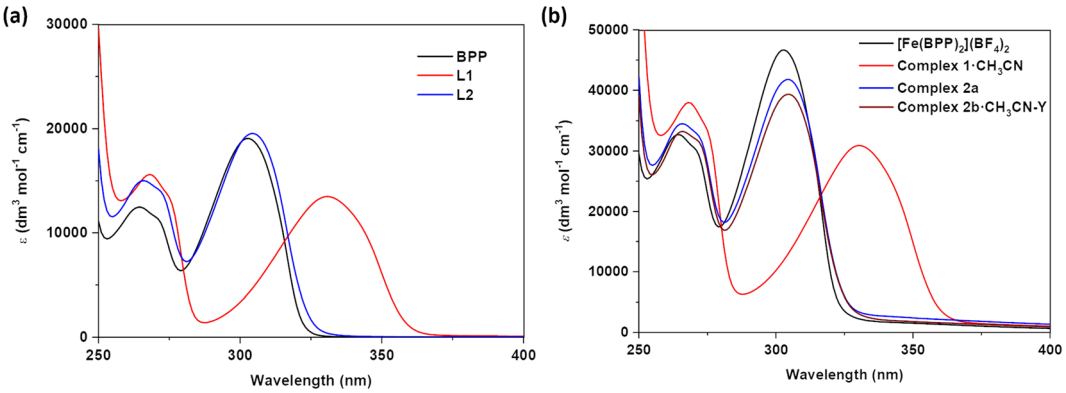

Fig. 2 Electronic absorption spectroscopic studies. UV-Vis electronic absorption spectra of (a) ligands and (b) complexes measured in acetonitrile solution. Functionalization of the parent BPP skeleton with COOEt substituent caused bathochromic shifting of the absorption maxima of **L2**, whereas OCH_2COCH_3 substituent caused no such shift in **L2**.

Electronic absorption spectra of ligands L1 and L2 and complexes 1·CH_3CN, 2a, and 2b·CH_3CN-Y

To get insights into the effect of substituents on the absorption spectroscopic characteristics of ligands and complexes, UV-Vis absorption spectroscopic studies of **L1**, **L2**, **1**·CH_3CN, **2a**, and **2b**·CH_3CN-Y were performed in acetonitrile solvent. To make comparisons, spectroscopic studies of the parent BPP ligand and its complex—$[Fe(BPP)_2](BF_4)_2$—were also performed. In general, two sets of transitions in the 250-to-275 nm and 275-to-400 nm regions were observed for the ligands and their corresponding complexes (Fig. 2 and Table 1). The first and second set of transitions are tentatively attributed to the $\pi \rightarrow \pi^*$ and $n \rightarrow \pi^*$ transitions of the ligand skeletons. The absorption maxima of BPP and **L2** are comparable, elucidating the negligible electronic effect of the OCH_2COCH_3 substituent on the BPP skeleton. On the other hand, absorption maxima of **L1** were bathochromically shifted relative to the parent BPP ligand, reflecting on the significant inductive effect of the COOEt substituent on the BPP skeleton. We tentatively attribute the bathochromic shifting observed for **L1**, relative to BPP, to the stabilization of the lowest unoccupied molecular orbital (LUMO) of the ligand imparted by the electron withdrawing COOEt substituent. Complexation of the ligands with iron(II) induced negligible changes in the absorption characteristics of the ligands, as inferred from the comparable nature of the absorption maxima of the ligands and their corresponding complexes (Fig. 2a and b). Remarkably, for **1**·CH_3CN, a shoulder with a maximum centred at 461 nm was observed (Fig. S7†), attributed to the singlet metal-to-ligand charge transfer (^{1}MLCT) transition associated with the LS form of the complex. Such a transition was not observed for $[Fe(BPP)_2](BF_4)_2$, complexes **2a**, and **2b**·CH_3CN-Y, indicating the HS state of the complexes in the solution.

Table 1 Absorption maxima ($\lambda_{max.}$) and molar absorption coefficients (ε) of ligands and complexes in CH_3CN

Entry	$\lambda_{max.}$ (CH_3CN)/nm (ε)/dm^3 mol^{-1} cm^{-1}
BPP	265 (12 567), 272 (11 399), 303 (19 136)
L1	268 (15 711), 275 (13 559), 331 (13 559)
L2	265 (15 008), 272 (13 884), 304 (19 654)
$[Fe(BPP)_2](BF_4)_2$	264 (32 791), 271 (30 011), 302 (46 736)
1·CH_3CN	268 (38 147), 274 (33 538), 330 (30 875), 461 (708)
2a	265 (34 708), 272 (32 440), 304 (41 893)
2b·CH_3CN-Y	265 (33 216), 272 (31 577), 304 (39 479)

Structural studies of L1; low spin (LS) and high spin (HS) forms of complex 1·CH_3CN; HS form of 2a; LS form of 2b·CH_3CN-R; and LS and HS forms of 2b·CH_3CN-Y

Slow evaporation of the $CDCl_3$ solution of **L1** in an NMR tube resulted in the formation of single crystals of **L1** suitable for X-ray diffraction (XRD) studies (Table S1†). In the molecular structure shown in Fig. 3a, the coordinating β-nitrogens of the pyrazole rings are in the *trans* position with respect to the pyridyl nitrogen, in line with the previously reported structures of bpp-based ligands.[37–39] The *trans* orientation of the nitrogen atoms indicates the need for the rotation of the pyrazole rings to coordinate with iron(II) centres.

Structure determination of wine-red crystals at 173 K (Fig. 3b and Table S2†) and 300 K (Fig. S8 and Table S1†) obtained from the reaction between **L1** and iron(II) salt revealed that complex **1**·CH_3CN crystallized with one lattice acetonitrile solvent. The iron(II) centres in the crystals are in the LS state as inferred from the Fe–N bond lengths and angular parameters summarized in Tables 2 and S3.† We have also obtained the HS structure of **1**·CH_3CN at 345 K (Fig. 3c and Table S2†) from a LS **1**·CH_3CN crystal by heating it in the diffractometer at a rate of 0.5 K min^{-1}.

A comparison between the structures of the LS and HS forms **1**·CH_3CN indicates that the spin-state switching is accompanied by conformational switching of one of the ethyl substituents (Fig. 3b and c) and pronounced angular distortion (Table 2 and Fig. 3d). Noteworthy are the *trans-N*{pyridyl}-Fe–N{pyridyl} angle (ϕ), *N*{pyrazolyl}-Fe–N{pyrazolyl} clamp angle (ψ), average of four *cis-N*{pyridyl}-Fe–N{pyrazolyl} angles (α), distortion index (Σ),[40] angle between the planes of two ligands

This journal is © The Royal Society of Chemistry 2024

Open Access Article. Published on 22 May 2024. Downloaded on 9/16/2024 9:40:39 PM.
This article is licensed under a Creative Commons Attribution 3.0 Unported Licence.

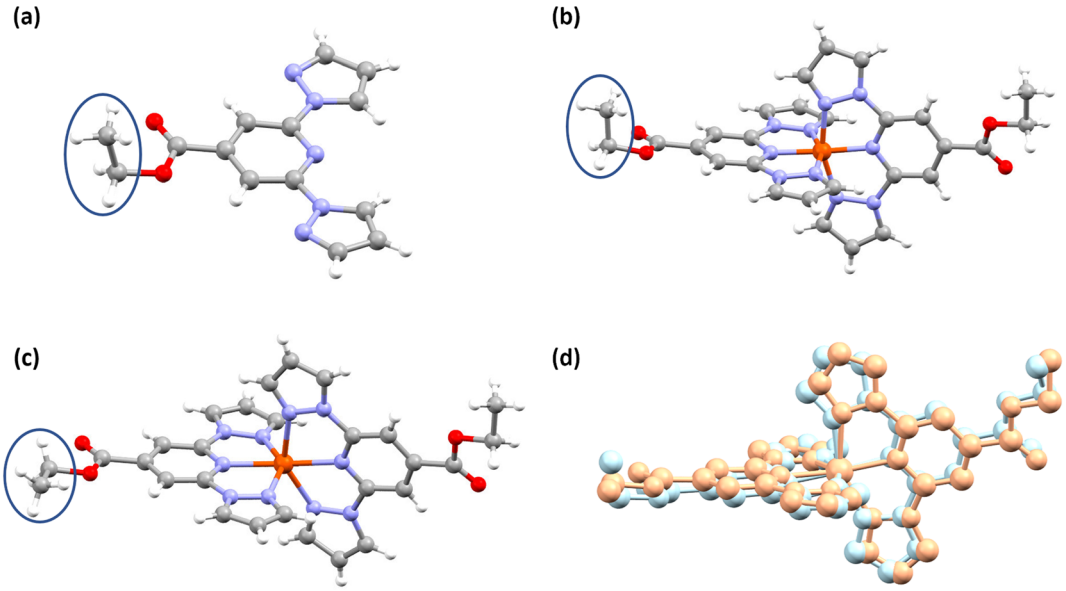

Fig. 3 Structures of **L1** and the corresponding complex—**1**·CH_3CN—obtained from single-crystal X-ray diffraction (SC-XRD) studies. Molecular structures of (a) **L1**, (b) LS- and (c) HS-forms of complex **1**·CH_3CN, and (d) overlay of LS (light blue) and HS (light orange) structures of **1**·CH_3CN determined at 300 K and 345 K, respectively. The lattice acetonitrile molecules and BF_4^- anions in b–d are not shown for clarity. The most abundant parts of the disordered moieties are shown for b and c. Colour code: white, hydrogen; grey, carbon; blue, nitrogen; red, oxygen; orange, iron. The blue circles in a–c indicate the positions of one of the ethyl groups of the COOEt substituents in **L1** and the corresponding complex in the LS and HS states. The LS-to-HS switching of **1**·CH_3CN involves pronounced angular distortion and conformational switching of the circled ethyl groups. Such structural variations associated with the LS and HS forms of **1**·CH_3CN cause bi-stable spin-state switching of the complex, as discussed below.

Table 2 Fe–N bond lengths (Å) and angular parameters (°) of the LS and HS forms of **1**·CH_3CN, HS form of **2a**, and LS and HS forms of **2b**·CH_3CN-Y

Parameter	**1**·CH_3CN (LS)	**1**·CH_3CN (HS)	**2a** (HS)	**2b**·CH_3CN-Y (LS)	**2b**·CH_3CN-Y (HS)
T/K	173	345	173	120	300
rFe–N	1.942	2.161	2.177	1.952	2.160
N_3–Fe_1–N_8 (ϕ)	172.87	159.20	168.75	177.37	178.68
N_6–Fe_1–N_{10} (ψ)	160.53	145.15	146.01	159.7	147.63
N_1–Fe_1–N_5 (ψ)	160.43	145.32	145.15	159.87	147.29
α	80.29	72.94	72.79	79.89	73.74
Σ	84.40	158.67	160.10	89.58	148.09
θ	86.70	80.73	84.67	85.86	85.00
Θ	315.18	637.22	540.14	294.20	474.74

(θ), and trigonal distortion parameter (Θ), as shown in Table 2. Upon LS-to-HS switching, significant deviation from close to octahedral-to-trigonal prismatic structure has been observed for **1**·CH_3CN.

Structural investigation of complex **2a** obtained at 173 K indicates that the complex is in the HS form. The complex cation (Fig. 4a and Table S4†) is distorted, as inferred from the angular parameters listed in Table 2. However, the distortion is less pronounced in HS-**2a** relative to HS-**1**·CH_3CN. In the case of **2b**·CH_3CN-Y, the LS and HS forms of the complex (Fig. 4b and c and Table S4†) showed no appreciable deviation of ϕ value from the ideal value of 180° (Table 2). Other angular parameters associated with the LS and HS forms of **2b**·CH_3CN-Y are comparable with the respective ones obtained for the LS and HS forms of **1**·CH_3CN. A notable exception is the Σ value, which is relatively larger for the LS **2b**·CH_3CN-Y than the one obtained for the LS **1**·CH_3CN. Conversely, the Σ value of the HS **1**·CH_3CN is found to be greater than the value obtained for the HS **2b**·CH_3CN-Y. Overall, the variation of Σ upon spin-state switching is larger for **1**·CH_3CN relative to **2b**·CH_3CN-Y, indicating the fact that the former complex follows a more distorted pathway than the latter upon spin-state switching.

The red polymorph of **2b**, **2b**·CH_3CN-R, also crystallized with lattice acetonitrile solvent. See Table S5† for the structural data. The polymorph is in the LS state at 173 K as inferred from the molecular structure (Fig. 4d) and angular parameters (Table S6†) obtained from SC-XRD studies. The average of Fe–N bond lengths and angular parameters of **2b**·CH_3CN-R are comparable with the values obtained for the LS **2b**·CH_3CN-Y, as listed in Table S6.†

For complex **1**·CH_3CN in the HS and LS states, the complex cations in the crystal lattice organize in a pseudo 1D-chain like manner along the c-axis (Fig. S9 and S11†). The pseudo

Open Access Article. Published on 22 May 2024. Downloaded on 9/16/2024 9:40:39 PM.
This article is licensed under a Creative Commons Attribution 3.0 Unported Licence.

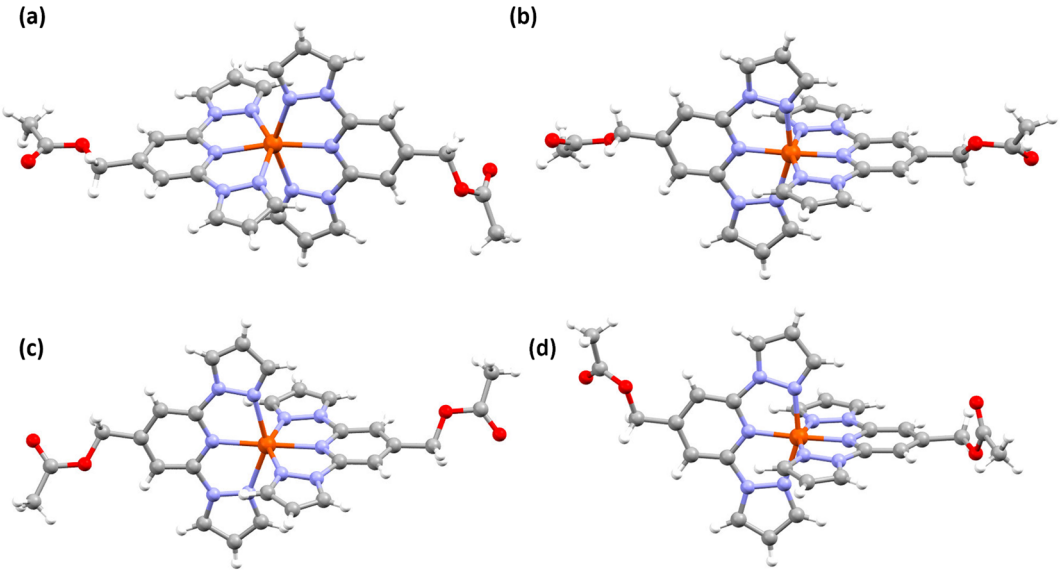

Fig. 4 Molecular structures of complexes composed of **L2** obtained from single-crystal X-ray diffraction (SC-XRD) studies. (a) HS form of complex **2a**, (b) LS form of complex **2b**·CH_3CN-Y, (c) HS form of complex **2b**·CH_3CN-Y, and (d) LS form of **2b**·CH_3CN-R. The lattice acetonitrile molecules, where appropriate, and counter anions are not shown for clarity. Colour code: white, hydrogen; grey, carbon; blue, nitrogen; red, oxygen; orange, iron.

1D-chains stack (inter-sheet organization) along the crystallographic *b*-plane. Molecular organization in the lattices is governed by intermolecular interactions between the complex cation, counter anion, and acetonitrile solvent entities as depicted in Fig. S10 and S12.† Noteworthy are the short contacts between the lattice acetonitrile solvent and the complex cation (see Table S7† for details).

For complex **2a** in the HS form, complex cations are ordered in an alternative manner along the *b*- and *c*-axes (Fig. S13†). Short contacts between F atoms of the counter cation and H atoms of the pyridine/pyrazole moieties along with an O–H contact, involving carbonyl oxygen of the –COOEt substituent and pyrazole-based hydrogen atom, between adjacent complex cations direct the molecular organization in the lattice (Fig. S14 and Table S8†). In the cases of the HS and LS forms of **2b**·CH_3CN-Y, a zig-zag molecular organization (Fig. S15 and S17†) in the crystal lattice is observed, when viewed along the crystallographic axis *a*. The lattice is held together by inter molecular contacts between the counter anion and complex cation (see Fig. S16 and S18 and Tables S9† for details). Similar molecular organization (Fig. S19†) and intermolecular contacts (Fig. S20 and Table S10†), as in **2b**·CH_3CN-Y, are observed in the crystal lattice of LS **2b**·CH_3CN-R.

For the estimation of short contacts, the criterion $d(x...y) = \sum r(\mathrm{vdW})[x, y] - 0.2$ Å was used, where $d(x...y)$ is the distance between two atoms and $\sum r(\mathrm{vdW})[x, y]$ is the sum of van der Waals radii of atoms *x* and *y*. Note, the short contact estimation following the above criterion is associated with significant pitfalls as discussed by G. P. Schiemenz.[41] Considering the above point, the discussion presented in this study mainly intends to elucidate how intermolecular short contacts direct the molecular organization in the crystal lattices of complexes discussed in this study.

Spin-state switching characteristics of 1·CH_3CN and 2b·CH_3CN-Y and magnetic studies of HS 2a

Magnetic susceptibility measurements of gently ground crystals of **1**·CH_3CN, **2a**, and **2b**·CH_3CN-Y were performed under 0.1 T applied magnetic field at a scan rate of 3 K min^{-1}. Complex **1**·CH_3CN exhibited an abrupt SCO with 44 K and 52 K hysteresis loops for the first ($T_{1/2\uparrow}$ = 320 K and $T_{1/2\downarrow}$ = 276 K) and second ($T_{1/2\uparrow}$ = 320 K and $T_{1/2\downarrow}$ = 268 K) cycles, respectively, as depicted in Fig. 5a.

The obtained χT products of 3.18 cm^3 K mol^{-1} and 0.18 cm^3 K mol^{-1} at 335 K and 200 K, respectively, for the first cycle (Table 3), indicate the presence of pure HS and predominantly LS states of the complex at those temperatures. The above point elucidates temperature-induced spin state switching of **1**·CH_3CN. Upon repeated scanning, a steady decrease of χT values was observed until the 11th scan (Fig. 5b). Starting from the 12th cycle, a relatively stabilized χT *versus* *T* plots were observed (Fig. 5b). This is attributed to the trapping of the sample in a mixed spin phase composed predominantly of the LS state.[42] The cycling is also accompanied by a steady increase of the χT value in the 5 K-to-275 K region, as recently observed for an iron(II)-BPP system reported by Halcrow and co-workers.[43] A fraction of the complex molecules in the mixed phase, obtained after the 11th cycle, undergoes SCO, as depicted in Fig. 5b.

To check for the effect of *in situ* solvent removal on the spin-state switching characteristics of **1**·CH_3CN, the sample was annealed in the SQUID chamber at 400 K for thirty minutes. A cool–heat cycle performed after the annealing step

 This journal is © The Royal Society of Chemistry 2024

Open Access Article. Published on 22 May 2024. Downloaded on 9/16/2024 9:40:39 PM.
This article is licensed under a Creative Commons Attribution 3.0 Unported Licence.

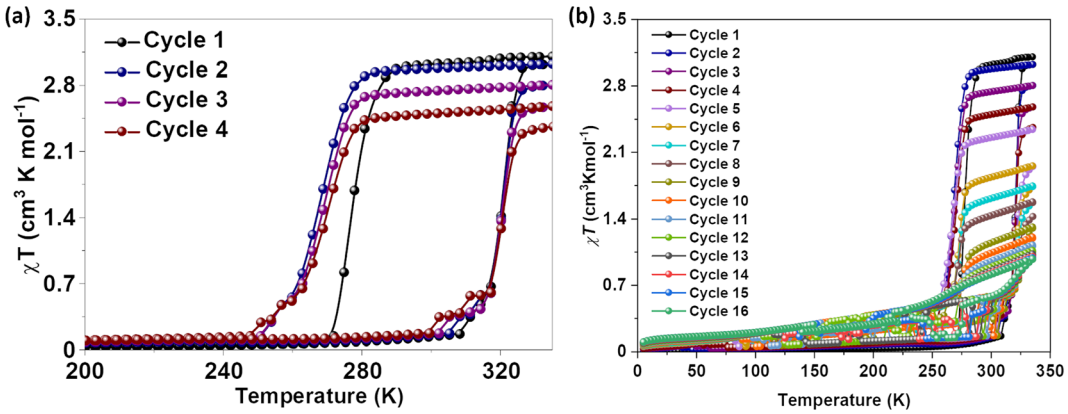

Fig. 5 Temperature-induced spin-state switching characteristics of **1**·CH_3CN. (a) χT *versus* T plots of wine-red crystals of **1**·CH_3CN measured at a scan rate of 3 K min^{-1}. The sample showed bi-stable—abrupt and hysteretic—spin-state switching with $\Delta T_{1/2}$ = 44 K and $T_{1/2}$ = 298 K in the first cycle. (b) Repeated heat–cool cycling resulted in the decrease of χT values with a concomitant increase of thermal hysteresis width due to the stabilization of the HS state in the cooling mode. Spin-state switching in **1**·CH_3CN is accompanied by pronounced angular distortion, see Table 2, with concomitant self-grinding of the crystals, causing cycle-dependent evolution of the switching characteristics.

Table 3 Parameters associated with the SCO of **1**·CH_3CN obtained from SQUID and DSC studies. Scan rates of 3 K min^{-1} and 2 K min^{-1} were used for the SQUID and DSC measurements, respectively

	SQUID (sample 1)			DSC (sample 1)	
	χT (HS)/cm^3 K mol^{-1}	$T_{1/2}$/K	ΔT/K	$T_{1/2}$/K	ΔT/K
Cycle 1	3.18	298	44	298	44
Cycle 2	3.02	294	52	294	56
Cycle 3	2.79	294	51	293	60
Cycle 4	2.56	295	50	292	66

revealed that the sample is trapped in the HS state, as depicted in Fig. S21.† The results obtained from continuous cycling depicted in Fig. 5 elucidate that spin-state switching induces self-grinding in the lattice, causing the spin-state switching to become unstable upon repeated cycling. On the other hand, the purposeful removal of the lattice solvent in the SQUID sample chamber traps the complex in the HS state, demonstrating the helping hand of the lattice solvent in mediating spin-state switching.

To check for the reproducible nature of the switching process and the effect of scan rate on the switching characteristics, we have prepared a second batch of **1**·CH_3CN crystals and probed their spin-state switching characteristics. When measured at a scan rate of 3 K min^{-1}, the sample underwent temperature-induced bi-stable spin-state switching (Fig. S22†) with a thermal hysteresis width of 48 K and $T_{1/2}$ = 298 K ($T_{1/2\uparrow}$ = 322 K and $T_{1/2\downarrow}$ = 274 K). Such results are comparable with the values obtained from the data shown in Fig. 5a (cycle 1). When a crop of fresh crystals obtained from the second batch was studied at a scan rate of 1 K min^{-1} (Fig. S23†), a thermal hysteresis width of 41 K and $T_{1/2}$ = 304 K ($T_{1/2\uparrow}$ = 325 K and $T_{1/2\downarrow}$ = 284 K) were obtained. While the $T_{1/2}$ obtained for the heating branch is comparable to the previous results, the $T_{1/2}$ obtained for the cooling branch markedly differs from that of others. We attribute this difference to the nature of the sequence employed to collect the data. In previous cases, the data were collected from 340 K after keeping the sample at that temperature for thirty minutes in the SQUID chamber, see the Experimental section (S1†) for details. On the other hand, the first cooling branch at 1 K min^{-1} scan rate was obtained after the first heating branch (Fig. S23†). Such an experimental protocol could have caused a slightly different grinding of the crystals upon spin-state switching. Overall, the reproducible nature of bi-stable spin-state switching in complex **1**·CH_3CN is unambiguously elucidated by studying the switching properties of two different batches of the complex.

To check for the LIESST[44] active nature of **1**·CH_3CN, we have prepared a third batch of crystals. Prior to photomagnetic studies, the sample was cooled to 5 K at a scan rate of 3 K under an applied field of 0.1 T. The subsequent irradiation of the complex using red laser light (λ = 637 nm, laser intensity was adjusted to 10 mW cm^{-2}) caused an increase of the magnetic moment (Fig. 6a, grey solid circles). A gradual increase of the χT value was observed under laser irradiation. After three hours, χT = about 1 cm^3 K mol^{-1} was obtained, indicating that about 28% of the iron(II) centres are switched to the HS state caused by the LIESST effect and no further increase in the χT value was observed after that. Temperature-dependent investigation of the photoexcited metastable HS fraction in the absence of the laser irradiation resulted in a gradual decrease of χT value in two steps, ultimately reaching values typical of the LS state of the compound at 100 K. The gradual nature of the LIESST curve precluded the determination of specific T(LIESST) temperatures. The heat–cool cycles of the sample performed after the LIESST study indicate that the cooperative spin-state switching is preserved in the sample (Fig. 6a). The $T_{1/2}$ = 305 K and $\Delta T_{1/2}$ = 42 K (Table S11†) obtained for the batch in the first cycle (scan rate = 3 K min^{-1}) are comparable to the values obtained for the second batch of the complex

Open Access Article. Published on 22 May 2024. Downloaded on 9/16/2024 9:40:39 PM.
This article is licensed under a Creative Commons Attribution 3.0 Unported Licence.

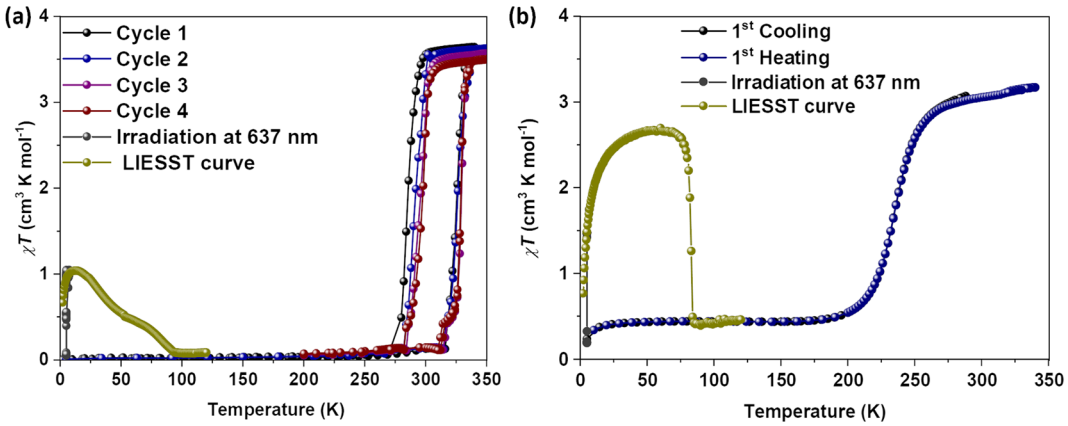

Fig. 6 Temperature- and light-induced spin-state switching of **1**·CH_3CN and **2b**·CH_3CN-Y. (a) χT *versus* T plots of wine-red crystals of **1**·CH_3CN measured at a scan rate of 3 K min^{-1}, showing temperature-dependent spin-state switching. Upon irradiation with 637 nm light at 5 K, the complex underwent light-induced LS-to-HS switching (grey filled circles) due to the LIESST effect. The green filled circles represent the temperature-dependent switching of the metastable HS state to the LS state. (b) χT *versus* T plot of complex **2b**·CH_3CN-Y—the complex shows a gradual temperature-induced spin-state switching ($T_{1/2}$ = 234 K) with no thermal hysteresis. The complex also undergoes light-induced LS-to-HS switching (black filled circles), when irradiated with 637 nm light at 5 K. Temperature-induced conversion of the metastable HS state to the LS state starts around 50 K (green solid circles). A point noteworthy here is not only the thermal switching but also LIESST-mediated SCO is influenced by the nature of substituent, elucidating a connection between structural and spin isomerism.

measured at a scan rate of 1 K min^{-1} (Fig. S23†). See the discussion in the previous paragraph. This implies a dependence of SCO parameters on the measurement protocol: experiments performed by cooling the HS sample from 340 K yielded $T_{1/2}$ = 298 K, whereas $T_{1/2}$ = 305 K was obtained when starting from the LS state.

Unlike **1**·CH_3CN, complex **2a** remained in the HS state upon cooling from 300 K to 5 K, as inferred from the χT *versus* T plot shown in Fig. S24.† This observation is consistent with the HS state of solvent-free complex **1**, indicating the role of lattice solvent in mediating spin-state switching. At 300 K, the χT value of 3.98 cm^3 K mol^{-1} was obtained. The value is larger than the spin only value (3 cm^3 K mol^{-1}) expected for an isolated HS iron(II) centre with S = 2 and L = 0. Upon cooling, the χT value remained almost constant until 50 K and then decreased to 0.95 cm^3 K mol^{-1} at 1.8 K. As far as HS iron(II) systems are concerned, such a drop could be attributed to the depopulation of excited stark levels of the ground-state multiplet, presence of magnetic anisotropy, and intermolecular antiferromagnetic interactions. Considering the mononuclear nature of the complex and the shortest inter iron–iron distance of 8.69(4) Å in the crystal lattice, the contribution from intermolecular antiferromagnetic interactions is ruled out.

On the other hand, the steep decrease observed for **2a** at low temperatures could be due to the presence of magnetic anisotropy. To clarify this point, we have performed isothermal field (M) *versus* magnetization (H) and alternating current (AC) magnetic susceptibility measurements. Isothermal M *versus* H data (Fig. S25a†) collected in the temperature range of 2 to 10 K until 7 T revealed that magnetization curves (M *versus* H/T, see Fig. S25b†) are non-superimposable, especially in the high-field regime. Such observation along with the magnetization values of 3.24μ_B (2 K) at 7 T indicates the possible presence of magnetic anisotropy in the complex. To probe the existence of slow relaxation of magnetization in the complex, AC measurements at zero and applied DC magnetic fields were performed at 1.8 K. Unfortunately, no out-of-phase susceptibility peaks (χ'') were observed either at zero or applied DC fields (Fig. S26†), indicating that complex **2a** is not a single-molecule magnet (SMM) at and above 1.8 K. This result is not surprising considering the fact that iron(II)-based SMMs are not frequently observed[45] due to efficient quantum tunnelling of magnetization facilitating fast under barrier magnetization relaxation.

Magnetic measurements of compound **2b**·CH_3CN-Y revealed temperature-induced SCO behavior below room temperature (Fig. 6b). The complex is in the LS state in the 5-to-175 K temperature range. The χT value of about 0.40 cm^3 K mol^{-1} in the temperature range is indicative of a remnant HS fraction. Heating the sample above 175 K resulted in a gradual LS-to-HS switching. The χT value of 3.17 cm^3 K mol^{-1} was obtained at 340 K, in the range expected for a mononuclear iron(II) complex in the HS state. The cooling branch retraced the heating branch, and no thermal hysteresis was observed. For **2b**·CH_3CN-Y, $T_{1/2}$ = 234 K was obtained, and the value is in the range reported for BPP-based iron(II) complexes. Irradiation of **2b**·CH_3CN-Y at 5 K with a red laser (λ = 637 nm) induced LS-to-HS switching as a consequence of the LIESST effect. After three hours of irradiation, χT = 1.5 cm^3 K mol^{-1} was obtained; no further increase of the χT value was observed upon further irradiation. Heating of the metastable HS sample in the dark—that is, in the absence of laser irradiation—resulted in an increase of the χT value. At 50 K, χT = 2.7 cm^3 K mol^{-1} was obtained, indicating that approximately 85% of the iron(II) centers underwent LS-to-HS switching. Such an increase of the χT value, until 50 K, while heating the sample

 This journal is © The Royal Society of Chemistry 2024

Open Access Article. Published on 22 May 2024. Downloaded on 9/16/2024 9:40:39 PM.
This article is licensed under a Creative Commons Attribution 3.0 Unported Licence.

in the absence of light irradiation is attributed to the population of the zero-field split high energy stark levels of the HS term corresponding to the photoexcited metastable HS **2b**·CH_3CN-Y. Heating the sample above 50 K led to an abrupt decrease of the HS fraction back to the LS state, indicating the decay of the metastable HS state. T(LIESST) = 83 K is calculated for the complex from the minimum in the $\partial(\chi T)/\partial T$ *versus* T curve (data not shown). For the family of iron(II)-BPP complexes, the relation $T(\text{LIESST}) = 150 - 0.3T_{1/2}$ was established. Using the relation T(LIESST) = 80 K is calculated for **2b**·CH_3CN-Y, comparable with the experimental value of 83 K.

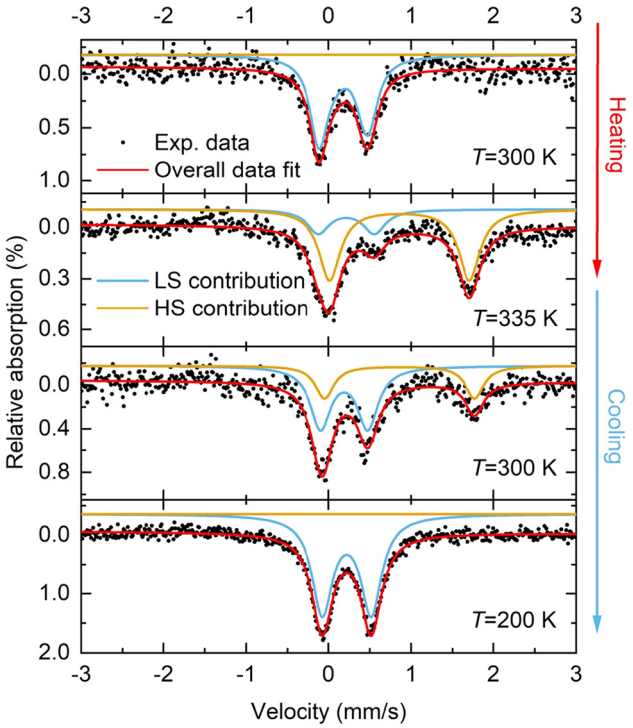

Fig. 7 Temperature-dependent ^{57}Fe Mössbauer spectroscopic studies of **1**·CH_3CN. The complex was heated from 300 to 335 K, leading to the observation of partial LS → HS switching: 74.6% HS and 25.4% LS. Cooling the sample back to 300 K resulted in the observation of a LS : HS mixture in a 67.3% : 32.7% ratio, indicating the hysteretic nature of the spin-state switching process. Cooling down to 200 K resulted in a pure LS state, in agreement with the magnetometry data. Note: 335 K is the maximum achievable temperature limit with the instrument used to collect the ^{57}Fe Mössbauer data.

This elucidates that there exists a linear dependence between T(LIESST) and $T_{1/2}$ for **2b**·CH_3CN-Y, as previously observed for iron(II) complexes composed of BPP-based and other ligand systems.[46]

^{57}Fe Mössbauer spectroscopic studies of 1·CH_3CN

In addition to the magnetometry measurements, ^{57}Fe Mössbauer spectroscopy measurements were performed on **1**·CH_3CN to obtain the spin state composition at different temperatures. Fig. 7 shows the temperature-dependent ^{57}Fe Mössbauer spectra of **1**·CH_3CN at 300 K and 335 K (heating) and 300 K and 200 K (cooling). The LS and HS contributions were fitted with two discrete doublets and the fit parameters obtained are given in Table 4. At 300 K, 100% LS state of the complex was inferred after fitting the data (Fig. 7 and Table 4). Upon heating to 335 K, the original LS doublet (300 K) lost intensity, and a second HS doublet with higher quadrupole and isomer shift forms. A composition of 74.6% HS and 25.4% LS was obtained based on the fitted resonant areas shown in Table 4. Upon cooling to 300 K, the spin-state equilibrium shifted towards the LS state and a LS : HS ratio of 67.3% : 32.7% was obtained. Further cooling to 200 K resulted in a complete spin state switching and the complex was found to be in 100% LS state.

The results obtained from the ^{57}Fe Mössbauer spectroscopic studies indicate the existence of hysteretic spin-state switching in **1**·CH_3CN, in agreement with the magnetic susceptibility measurements discussed above. However, a 100% HS state at 335 K (heating) and 300 K (cooling) was not observed in the ^{57}Fe Mössbauer spectroscopic studies. In line with the thermal behavior of the **1**·CH_3CN powder (see below), we attribute this discrepancy to the partial loss of lattice solvent during the Mössbauer studies, where the sample is kept above room temperature for several hours.

Solution-state spin-state switching characteristic of 1·CH_3CN

In addition to the magnetometry measurements performed on the crystalline form of **1**·CH_3CN, magnetometry studies of the complex in the solution phase were performed using a SQUID magnetometer. For the studies, a 7.42 mmol solution of the complex in acetonitrile was used.

Fig. 8 shows the mass magnetization as a function of temperature for three measured cycles. The inset shows the range from 180 to 360 K to highlight the observed thermal hysteresis. The measurement shows a much smaller thermal hysteresis

Table 4 Fitting parameters obtained from ^{57}Fe Mössbauer spectroscopic studies of **1**·CH_3CN. Fits were performed with two discrete doublets. δ is the isomer shift relative to α-Fe and ΔE_Q is the quadrupole splitting. The values were rounded to the third decimal

	LS doublet			HS doublet		
Temperature [K]	δ_{LS} [mm s^{-1}]	$\Delta E_{Q(LS)}$ [mm s^{-1}]	Resonant area [%]	δ_{HS} [mm s^{-1}]	$\Delta E_{Q(HS)}$ [mm s^{-1}]	Resonant area [%]
300	0.268	0.548	100	—	—	0
335	0.323	0.678	25.4	0.967	1.694	74.6
300	0.296	0.571	67.3	0.969	1.818	32.7
200	0.327	0.591	100	—	—	0

Open Access Article. Published on 22 May 2024. Downloaded on 9/16/2024 9:40:39 PM.
This article is licensed under a Creative Commons Attribution 3.0 Unported Licence.

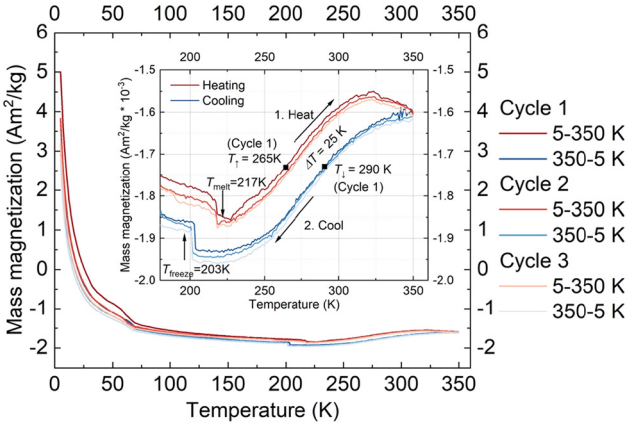

Fig. 8 Spin-state switching characteristics of **1**·CH_3CN in acetonitrile solution. Mass magnetization of acetonitrile solution of complex **1**·CH_3CN as a function of temperature at an applied magnetic field of 0.1 T. For the three heating–cooling cycles presented, the heating branch is shown in red, and the cooling branch is shown in blue, both going to brighter colours with a higher cycle number. Highlights, like the freezing and melting of the solvent, as well as $T_{\uparrow}$ = 265 K, $T_{\downarrow}$ = 290 K, and ΔT = 25 K (all cycle 1) are shown. In contrast to the measurement of the powder form of **1**·CH_3CN, the top branch is the heating branch, and the lower branch is the cooling branch, as labelled in the inset: 1. heat and 2. cool.

width than the one observed in the crystalline state with ΔT = 25 K ($T_{\uparrow}$ = 265 K, $T_{\downarrow}$ = 290 K) for the first cycle. In addition, the freezing and melting of the solvent acetonitrile were observed at T_{freeze} = 203 K and T_{melt} = 217 K, respectively. The thermal hysteresis remains almost the same for all the three cycles performed, indicating the absence of self-grinding in the solution phase. Such a result is contrary to the unstable nature of switching profiles obtained in the solid-state and elucidates the fact that stable hysteretic spin-state switching of the complex can be observed in the solution state.

At present, we are not clear about factors causing hysteretic SCO of **1**·CH_3CN in the solution state. Probable ones are aggregation of the complex in the solution and strong intermolecular interactions between the complex entity and acetonitrile solvent molecules.

Differential scanning calorimetric (DSC) and small- and wide-angle X-ray scattering (SWAXS) studies of 1·CH_3CN

To provide supplementary confirmation for the occurrence of temperature-induced spin-state switching in **1**·CH_3CN, differential scanning calorimetric (DSC) studies were performed, as shown in Fig. 9a. The $T_{1/2}$ and $\Delta T_{1/2}$ values obtained from the DSC studies (Table 3) are comparable with the values obtained from the χT *versus* T plots shown in Fig. 5a, confirming the bistable spin-state switching characteristic of **1**·CH_3CN.

Enthalpy (ΔH) and entropy (ΔS) variations associated with the LS-to-HS and HS-to-LS switching branches of the first cycle have also been estimated from the DSC plots shown in Fig. 9a. The estimated values of ΔH = 13.2 kJ mol^{-1} (LS-to-HS); 14.4 kJ mol^{-1} (HS-to-LS) and ΔS = 41.25 J mol^{-1} K^{-1} (LS-to-HS); 52.17 J mol^{-1} K^{-1} (HS-to-LS) are comparable with the values reported for iron(II) SCO complexes.[47,48] The differing values of thermodynamic parameters in the LS-to-HS and HS-to-LS switching branches are attributed to different vibrational modes associated with the LS and HS forms of **1**·CH_3CN.

We have also performed SWAXS studies of complex **1**·CH_3CN to get a glimpse of lattice variations during the spin-state switching process upon repeated cycling. As shown in Fig. 9b, the SWAXS pattern obtained from a ground sample of **1**·CH_3CN is comparable with the calculated pattern obtained from the single-crystal data of the LS crystal. This observation confirming the retainment of crystalline order in the ground sample is remarkable, considering the fact that **1**·CH_3CN crystals are ground prior to magnetic measurements. The differences between the SWAXS and calculated patterns obtained at 297 K and 173 K, respectively, are attributed to temperature- and grinding-induced variations of lattice parameters in relation with the displacement of the co-crystallized solvent. Indeed, grinding may strongly impact the structure[49] and even cause loss of crystallinity and transformation to an amorphous state, as we recently observed for complex **c** (Fig. 1).[35] Repeated heat–cool cycles of the ground **1**·CH_3CN caused an irreversible transformation of diffraction profiles, serving as the proof of the evolution of the crystalline phases during the repeated heat–cool cycling.

To shed light on the fate of lattice acetonitrile in **1**·CH_3CN during the repeated heat–cool cycling, thermogravimetric analyses (TGA) of various forms of the complex were performed. The crystalline **1**·CH_3CN underwent a 5% weight loss around 400 K, corresponding to the loss of one molecule of acetonitrile from the lattice (Fig. S27a†). The weight loss obtained from the TGA is comparable with the calculated value of 4.9% for a loss of one molecule of acetonitrile from the lattice. In contrast, no such weight loss is observed for a sample dried at 423 K (Fig. S27a†), revealing the complete removal of acetonitrile molecules from the lattice. TGA analysis of the sample obtained after SWAXS studies also showed a lack of pronounced weight loss (Fig. S27b†) observed for **1**·CH_3CN. Moreover, the TGA profiles of the deliberately desolvated sample at 423 K and the sample obtained after the repeated SWAXS measurements are comparable. From the above observations, we infer that repeated spin-state switching of **1**·CH_3CN is accompanied by a gradual loss of lattice acetonitrile molecules, forming a **1**·$x CH_3CN$ ($x < 1$) lattice with variable solvent content. Note that the solvent removal process during the SWAXS measurements is accelerated due to the *ex situ* heating and cooling of the sample, which is in contrast to the magnetic measurements performed inside a SQUID sample chamber, where the sample is repeatedly scanned under a low-pressure He-atmosphere without exposure to the external conditions. This implies that the switching-induced lattice solvent release could progress differently between magnetometry and SWAXS conditions.

The first synthesis of BPP-COOEt ligand used to prepare **1**·CH_3CN discussed in this study was reported almost 20 years ago.[36] However, the utility of the ligand to prepare iron(II)-

 This journal is © The Royal Society of Chemistry 2024

Open Access Article. Published on 22 May 2024. Downloaded on 9/16/2024 9:40:39 PM.
This article is licensed under a Creative Commons Attribution 3.0 Unported Licence.

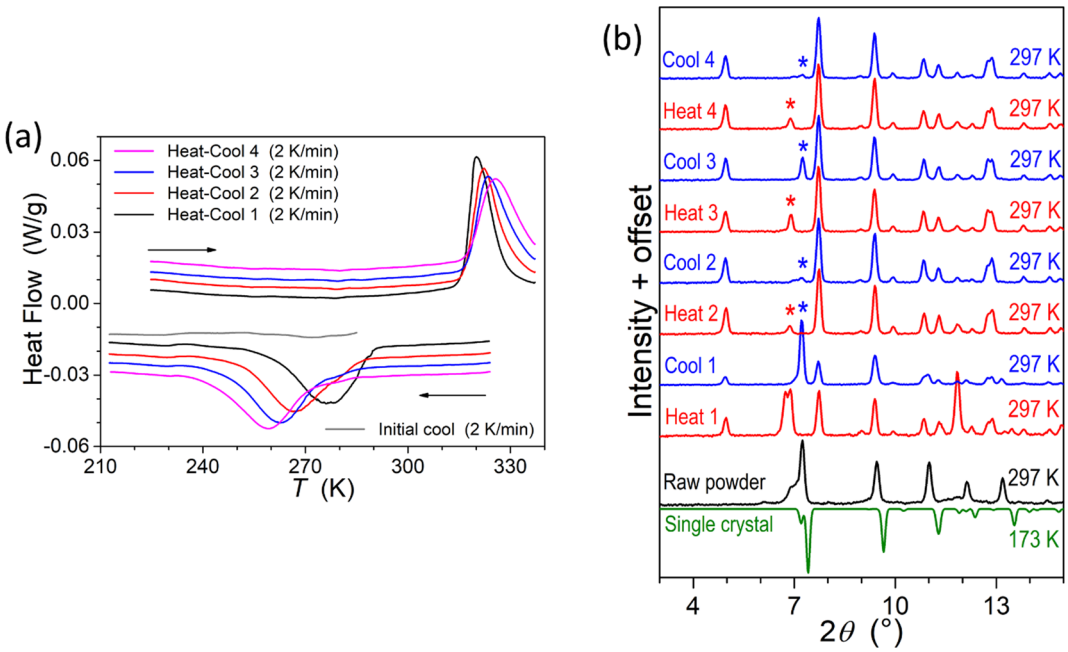

Fig. 9 Differential scanning calorimetric (DSC) and small- and wide-angle X-ray scattering (SWAXS) studies of complex **1**·CH_3CN. (a) DSC profiles showing temperature-induced spin-state switching in the 210-to-330 K temperature range. (b) SWAXS patterns of **1**·CH_3CN showing transitions between crystalline phases in response to repeated heat–cool cycling. The patterns were collected at 297 K after heating and cooling the sample *ex situ* at 330 K and 77 K, respectively. The irreversible changes in the SWAXS patterns obtained after repeated heat–cool cycling indicates that there exists phase variations contributing to the irreversible alteration of switching parameters, including the hysteresis width, upon repeated heat–cool cycling, as shown in Fig. 5b.

based mononuclear complexes was not reported until 2018.[34] The first reported iron(II) complex (**a**, Fig. 1) of the ligand, showed an irreversible LS-to-HS switching with the switching temperature centred around 330 K. Once heated above 350 K, complex **a** lost the lattice acetone solvent and the solvent-free version was trapped in the HS-state in the subsequent cooling. Our attempts to study similar complexes as acetonitrile (complex **b**; Fig. 1) and nitromethane (complexes **c** and **d**; Fig. 1) solvates led to the observation of hysteretic spin-state switching.[9,35] Remarkably, complex **c** showed stable hysteretic spin-state switching characteristics with $T_{1/2}$ = 288 K; $\Delta T_{1/2}$ = 62 K.[35]

In a different scenario, Sato and co-workers used BPP-COOEt to prepare a mononuclear cobalt(II) complex, which underwent switching of orbital angular momentum due to switching of coordination number from seven-to-six, and *vice versa*,[50] demonstrating an altogether different switching mechanism contrast to the spin-multiplicity-based switching demonstrated in this study. The above discussion indicates that coordination complexes based on a simple ligand system such as BPP-COOEt can feature exotic magnetic properties.

In a recent study, we observed pronounced molecular distortion upon spin-state switching of complexes **c** and **d** (Fig. 1 and Tables S12 and S13†).[35] Such distortion coupled with conformational variation of the Et group stabilizes the complexes either in a LS- or HS-state; creating an energy barrier, whereby thermal hysteresis loops are observed upon spin-state switching. Recently, Real and co-workers reported a mononuclear iron(II) complex with a wide 105 K thermal hysteresis loop and $T_{1/2}$ = 308 K. They elucidated that molecular distortion and conformational switching cause hysteretic spin-state switching of the complex.[4] The angular parameters collected in Table 3 reveal that the HS-form of complex **1**·CH_3CN features a distorted molecular geometry relative to its LS counterpart showing close to the ideal octahedral geometry. The obtained variations in ϕ and θ—$\Delta\phi$ = 13.67° and $\Delta\theta$ = 5.97°—indicate that the complex needs to traverse a significant energy barrier imposed by the crystal lattice to switch from one spin-state to another; that is, HS-to-LS and *vice versa*. Moreover, conformation of one of the ethyl groups of **1**·CH_3CN varies upon spin-state switching (Fig. 3b and c, blue circles). In the solid-state, positions of the ethyl groups of **L1** and LS form of **1**·CH_3CN are comparable as can be seen in Fig. 3a and b. To compare the structural variation coupled with spin-state switching in iron(II) complexes composed of BPP-COOEt ligands, we have compiled the difference between the angular parameters of the LS and HS forms of complexes **c**, **d**, and **1**·CH_3CN (Fig. 1) in Tables S12–S14.† All the complexes showed pronounced angular variation upon spin-state switching with HS forms of the complexes featuring large Θ values. Remarkably, the $\Delta\Theta$(LS–HS) values observed for **1**·CH_3CN (322.04°), **c** (302.07°), and **d** (318.22°) are the largest so far observed for BPP-based iron(II) complexes, surpassing the previous best of 215° reported by Halcrow and co-workers.[51]

Open Access Article. Published on 22 May 2024. Downloaded on 9/16/2024 9:40:39 PM.
This article is licensed under a Creative Commons Attribution 3.0 Unported Licence.

The successful determination of the structures of LS and HS forms of **1**·CH_3CN enabled us to compare the angular parameters obtained for the complex with the previously reported iron(II) complexes composed of BPP-based ligands and BPP-COOEt-based complexes (Fig. 10a). The task is made easy by Halcrow and co-workers, who have recently reported a compilation of angular parameters of LS and HS forms of iron(II)-BPP complexes and structural distortion pathways.[37] The authors have shown that a select band of HS-complexes (yellow squares in the pale grey region of Fig. 10b) that undergo strong angular distortion upon LS-to-HS switching are capable of showing abrupt and hysteretic spin-state switching.

The angular parameters obtained for the LS form of **1**·CH_3CN and the related complexes **c** and **d** are clustered together in Fig. 10a at the top right corner, as highlighted with a red circle. Similarly, the HS forms of the complexes—**1**·CH_3CN, **b**, **c**, and **d**—are also clustered in closer proximity, as highlighted with a yellow circle. Remarkably, the HS complexes fall in the pale grey region identified by Halcrow and co-workers (Fig. 10b), a position where an iron(II)-BPP complex is expected to show bi-stable SCO with sizable thermal hysteresis loop, albeit rarely. The above points elucidate that iron(II)-BPPCOOEt complexes belong to a not-frequently reported class of SCO systems featuring pronounced angular distortion and the consequent bi-stable spin-state switching.

In the case of HS complex **2a**, the angular parameters reveal a less distorted coordination geometry relative to its isomeric HS counterparts—**1**·CH_3CN, **b**, **c**, and **d**. As in Fig. 10a, the ϕ *versus* θ point is placed in the dark grey region of the angular landscape (Fig. 10b), where SCO is more probable relative to the structures in the pale grey region. However, complex **2a** remains stable in the HS state upon cooling. Such an observation is attributed to the lack of co-crystallized lattice solvent molecules aiding spin-state switching *via* elastic intermolecular interactions. This attribution is supported by the SCO active nature of the **2b**·CH_3CN-Y, crystallizing with lattice acetonitrile. The angular parameters associated with the LS and HS forms of **2b**·CH_3CN-Y (Table S15†) is placed in the dark grey region (Fig. 10a), where SCO is probable. Crucially, the lack of significant variation of the angular parameters between the HS and LS forms of **2b**·CH_3CN-Y and the gradual SCO accompanied with no thermal hysteresis serve as an additional proof of the contributing role of distortion in spurring bi-stable SCO in **1**·CH_3CN.

Overall, complex **1**·CH_3CN reported in this study is one of the remarkable mononuclear iron(II) spin-crossover complexes showing hysteretic spin-state switching with $T_{1/2}$ centred at RT. However, the SCO is lattice-solvent-dependent and significant variations in the lattice parameters, as inferred from the SWAXS studies, accompany the spin-state switching. Such aspects render the SCO unstable to thermal cycling, impeding the practical utility of the complex as a molecular switch or memory. On the other hand, the attribution that pronounced angular distortion and conformational variation of a functional group contribute to the opening of thermal hysteresis in **1**·CH_3CN adds to the extensive knowledge collected on SCO systems over almost a century. Remarkably, a direct proof of molecular distortion causing bi-stable SCO in **1**·CH_3CN can be obtained from the studies on **2b**·CH_3CN-Y. The HS form of the latter complex is significantly less distorted relative to the HS **1**·CH_3CN. Moreover, the gradual SCO of **2b**·CH_3CN-Y is accompanied with much smaller variations of the angular parameters relative to the ones obtained for **1**·CH_3CN.

As a perspective, the grand old phenomenon, SCO, continues to evolve keeping abreast with the contemporary developments in molecular magnetism and related topics.[5,52–63] It is our opinion, agreeing with the remarks made by the editors of this special collection, that the topic is fascinating to study, one of the pillars of molecular magnetism, and offers opportunities to perform basic science research,[64] allowing us chemists to elucidate how molecular structure variation imbues a

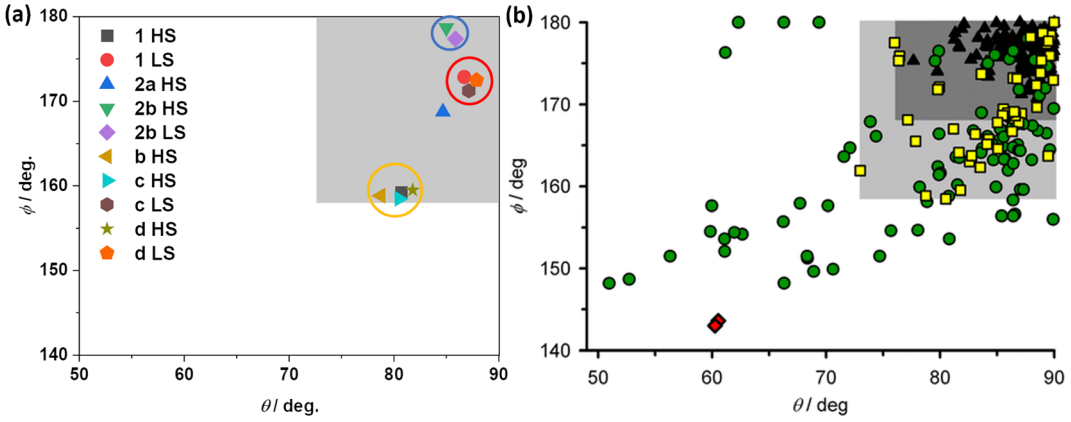

Fig. 10 Angular parameters of HS and LS states of iron(II)-BPP complexes. (a) Angular parameters of HS and LS forms of complexes **1**·CH_3CN, **b**, **c**, **d**, and **2b**·CH_3CN-Y. For complexes **b** and **2a** only HS structures are available, and the angular parameters obtained from the structures are shown. (b) A compilation of angular parameters reported for iron(II)-BPP complexes. (b) is reproduced from the study by Halcrow and co-workers.[37]
Copyright © 2024 The authors. Open access licensed under CC-BY 4.0.

Open Access Article. Published on 22 May 2024. Downloaded on 9/16/2024 9:40:39 PM.
This article is licensed under a Creative Commons Attribution 3.0 Unported Licence.

physical property change, as exemplified in this script relating molecular distortion with thermal hysteresis.

Conclusions

In this study, we show how structural isomerism influences spin isomerism. Complexes **1**·CH_3CN and **2a** featuring BF_4^- counter anions are a case. **1**·CH_3CN crystallizes with a lattice solvent and undergoes bi-stable spin state switching, whereas lattice solvent-free **2a** is trapped in the HS state, elucidating the helping hand of the co-crystallized lattice solvent in facilitating spin-state switching. Pronounced angular distortion and conformation variation of the ethyl substituent accompany spin-state switching of **1**·CH_3CN, causing a sizable thermal hysteresis width. As far as the angular parameters are considered, the HS form of **1**·CH_3CN features one of the largest reported values of the distortion parameter (Θ) comparable to the previously reported isostructural solvates (**b–c**, Fig. 1b) of the complex. The difference ($\Delta\Theta$) in the values of Θ estimated from the HS and LS structures of the complex series is also the largest reported for the iron(II)-BPP family of complexes. The perchlorate anion containing complex of **L2**—**2b**·CH_3CN—crystallizes as two polymorphs—**2b**·CH_3CN-Y and **2b**·CH_3CN-R. The switching in polymorph **2b**·CH_3CN-Y, crystallizing with lattice acetonitrile, is gradual and no hysteresis is observed. Analysis of the structures of the LS and HS forms of **2b**·CH_3CN-Y reveals that the *trans-N*{pyridyl}-Fe–N{pyridyl} angles (ϕ) are 177.37° and 178.68°, respectively. This indicates that switching in **2b**·CH_3CN-Y is accompanied by a small variation of ϕ and supports our hypothesis that a strong variation of ϕ upon spin-state switching contributes to the opening of the thermal hysteresis loop. Overall, the picture-perfect centering of the $T_{1/2}$ at 298 K and $\Delta T_{1/2}$ = 44 K observed for **1**·CH_3CN places the complex as one of the less frequently encountered mononuclear iron(II) complexes featuring bi-stable spin-state switching characteristics. The results are encouraging to pursue iron(II) complexes with a sizable thermal hysteresis width with $T_{1/2}$ centered in the vicinity of RT, a fundamental scientific quest in the topic.

Author contributions

S.K.K.: conceptualization, synthesis and characterization of the ligands and complexes, magnetic measurements, writing of the original and revised drafts, review and editing. A.M.: SC-XRD studies, review and editing. L.K.: ^{57}Fe Mössbauer and solution-phase magnetic studies and writing of the corresponding parts, review and editing. S.S.: solution-phase magnetic studies and review and editing. B.H.: SWAXS, TGA, and DSC studies, writing of the corresponding parts, review and editing. C.B.: SC-XRD studies, review and editing. I.S.: magnetic measurements, LIESST measurements, writing of the corresponding part, review and editing. H.W.: review and editing and funding acquisition. M.R.: review and editing and funding acquisition. All the authors have read and agreed to the submission of the manuscript.

Data availability

Crystallographic data for complexes **1**·CH_3CN and **2** have been deposited at the CCDC under 1560719 (**1**·CH_3CN, LS, 173 K); 2330938 (**1**·CH_3CN, LS, 300 K); 2330939 (**1**·CH_3CN, HS, 345 K); 1913041 (**2a**, HS, 173 K); 1953349 (**2b**·CH_3CN-R, LS, 173 K); 1953350 (**2b**·CH_3CN-Y, LS, 120 K); 2340087 (**2b**·CH_3CN-Y, HS, 300 K). The data can be obtained from the Cambridge Crystallographic Data Center.†

Conflicts of interest

The authors declare no conflicts of interest.

Acknowledgements

The authors thank Lydia Karmazin, University of Strasbourg, for the structure determination of **L1**. Grant Agency Innovation FRC is acknowledged for the financial support for the project self-assembly of spin-crossover (SCO) complexes on graphene. A. M. acknowledges the Alexander von Humboldt (AvH) Foundation for a postdoctoral fellowship, a Grant-in-Aid for the JSPS Research Fellowship program, and the financial support by JSPS KAKENHI Grant Numbers JP22KJ3097 and JP23K13723. M. R. thanks the DFG Priority Program 1928 "COORNETS" for generous support. L. K. and H. W. acknowledge the funding by the Deutsche Forschungsgemeinschaft (DFG, German Research Foundation) – Project-ID 278162697 – CRC 1242, Project A05. S. S. and H. W. acknowledge the financial support by the German Research Foundation (DFG) *via* the CRC/TRR 247 (Project-ID 388390466, sub-project B02). The authors thank Ulrich von Hörsten for his technical assistance with the ^{57}Fe Mössbauer spectroscopy measurements. I. S. acknowledges the Slovak (Slovak Research and Development Agency: APVV-19-0087, APVV-22-0172, DS-FR-22-0010 and Scientific Grant Agency of the Ministry of Education of Slovak Republic VEGA 1/0029/22) and Czech (Grant Agency of the Czech Republic No. 22-23760S) grant agencies for the financial support. The authors thank Karlsruhe Institute of Technology (KIT) for providing open access of the article through programme DEAL.

References

1 O. Sato, *Nat. Chem.*, 2016, **8**, 644–656.
2 R. Sessoli, D. Gatteschi, A. Caneschi and M. A. Novak, *Nature*, 1993, **365**, 141–143.
3 N. Ishikawa, M. Sugita, T. Ishikawa, S. Koshihara and Y. Kaizu, *J. Am. Chem. Soc.*, 2003, **125**, 8694–8695.

Open Access Article. Published on 22 May 2024. Downloaded on 9/16/2024 9:40:39 PM. This article is licensed under a Creative Commons Attribution 3.0 Unported Licence.

4 M. Seredyuk, K. Znovjyak, F. J. Valverde-Muñoz, I. da Silva, M. C. Muñoz, Y. S. Moroz and J. A. Real, *J. Am. Chem. Soc.*, 2022, **144**, 14297–14309.
5 S.-G. Wu, L.-F. Wang, Z.-Y. Ruan, S.-N. Du, S. Gómez-Coca, Z.-P. Ni, E. Ruiz, X.-M. Chen and M.-L. Tong, *J. Am. Chem. Soc.*, 2022, **144**, 14888–14896.
6 G. Gallé, D. Deldicque, J. Degert, Th. Forestier, J.-F. Létard and E. Freysz, *Appl. Phys. Lett.*, 2010, **96**, 041907.
7 B. Weber, W. Bauer and J. Obel, *Angew. Chem., Int. Ed.*, 2008, **47**, 10098–10101.
8 S. Brooker, *Chem. Soc. Rev.*, 2015, **44**, 2880–2892.
9 K. Senthil Kumar, B. Heinrich, S. Vela, E. Moreno-Pineda, C. Bailly and M. Ruben, *Dalton Trans.*, 2019, **48**, 3825–3830.
10 O. Kahn, J. Kröber and C. Jay, *Adv. Mater.*, 1992, **4**, 718–728.
11 M. A. Halcrow, *Chem. Lett.*, 2014, **43**, 1178–1188.
12 B. Schäfer, C. Rajnák, I. Šalitroš, O. Fuhr, D. Klar, C. Schmitz-Antoniak, E. Weschke, H. Wende and M. Ruben, *Chem. Commun.*, 2013, **49**, 10986.
13 S. Horiuchi and Y. Tokura, *Nat. Mater.*, 2008, **7**, 357–366.
14 A. S. Tayi, A. K. Shveyd, A. C.-H. Sue, J. M. Szarko, B. S. Rolczynski, D. Cao, T. J. Kennedy, A. A. Sarjeant, C. L. Stern, W. F. Paxton, W. Wu, S. K. Dey, A. C. Fahrenbach, J. R. Guest, H. Mohseni, L. X. Chen, K. L. Wang, J. F. Stoddart and S. I. Stupp, *Nature*, 2012, **488**, 485–489.
15 H. Liu, Y. Ye, X. Zhang, T. Yang, W. Wen and S. Jiang, *J. Mater. Chem. C*, 2022, **10**, 13676–13689.
16 S. Mohapatra, S. Cherifi-Hertel, S. K. Kuppusamy, G. Schmerber, J. Arabski, B. Gobaut, W. Weber, M. Bowen, V. Da Costa and S. Boukari, *J. Mater. Chem. C*, 2022, **10**, 8142–8167.
17 S. Horiuchi, Y. Tokunaga, G. Giovannetti, S. Picozzi, H. Itoh, R. Shimano, R. Kumai and Y. Tokura, *Nature*, 2010, **463**, 789–792.
18 W. Fujita and K. Awaga, *Science*, 1999, **286**, 261–262.
19 A. Paul, A. Gupta and S. Konar, *Cryst. Growth Des.*, 2021, **21**, 5473–5489.
20 A. Mizuno, R. Matsuoka, T. Mibu and T. Kusamoto, *Chem. Rev.*, 2024, **124**, 1034–1121.
21 Z. Hu, Y. Wang, A. Ullah, G. M. Gutiérrez-Finol, A. Bedoya-Pinto, P. Gargiani, D. Shi, S. Yang, Z. Shi, A. Gaita-Ariño and E. Coronado, *Chem*, 2023, **9**, 3613–3622.
22 C. A. P. Goodwin, F. Ortu, D. Reta, N. F. Chilton and D. P. Mills, *Nature*, 2017, **548**, 439–442.
23 F.-S. Guo, B. M. Day, Y.-C. Chen, M.-L. Tong, A. Mansikkamäki and R. A. Layfield, *Science*, 2018, **362**, 1400–1403.
24 P. Gütlich, *Eur. J. Inorg. Chem.*, 2013, **2013**, 581–591.
25 A. Dürrmann, G. Hörner and B. Weber, *Cryst. Growth Des.*, 2023, **23**, 1743–1754.
26 M. Paez-Espejo, M. Sy and K. Boukheddaden, *J. Am. Chem. Soc.*, 2018, **140**, 11954–11964.
27 R. Torres-Cavanillas, M. Gavara-Edo and E. Coronado, *Adv. Mater.*, 2024, **36**, 2307718.
28 V. Rubio-Giménez, S. Tatay and C. Martí-Gastaldo, *Chem. Soc. Rev.*, 2020, **49**, 5601–5638.
29 G. Molnár, S. Rat, L. Salmon, W. Nicolazzi and A. Bousseksou, *Adv. Mater.*, 2018, **30**, 1703862.
30 R. W. Hogue, S. Singh and S. Brooker, *Chem. Soc. Rev.*, 2018, **47**, 7303–7338.
31 M. A. Halcrow, *Chem. Soc. Rev.*, 2011, **40**, 4119.
32 J. M. Holland, C. A. Kilner, M. Thornton-Pett, M. A. Halcrow, J. A. McAllister and Z. Lu, *Chem. Commun.*, 2001, 577–578.
33 M. A. Halcrow, *Coord. Chem. Rev.*, 2009, **253**, 2493–2514.
34 V. García-López, M. Palacios-Corella, A. Abhervé, I. Pellicer-Carreño, C. Desplanches, M. Clemente-León and E. Coronado, *Dalton Trans.*, 2018, **47**, 16958–16968.
35 N. Suryadevara, A. Mizuno, L. Spieker, S. Salamon, S. Sleziona, A. Maas, E. Pollmann, B. Heinrich, M. Schleberger, H. Wende, S. K. Kuppusamy and M. Ruben, *Chem. – Eur. J.*, 2022, **28**, e202103853.
36 T. Vermonden, D. Branowska, A. T. M. Marcelis and E. J. R. Sudhölter, *Tetrahedron*, 2003, **59**, 5039–5045.
37 I. Capel Berdiell, E. Michaels, O. Q. Munro and M. A. Halcrow, *Inorg. Chem.*, 2024, **63**, 2732–2744.
38 S. K. Kuppusamy, A. Mizuno, A. García-Fuente, S. Van Der Poel, B. Heinrich, J. Ferrer, H. S. J. Van Der Zant and M. Ruben, *ACS Omega*, 2022, **7**, 13654–13666.
39 I. Šalitroš, O. Fuhr, M. Gál, M. Valášek and M. Ruben, *Chem. – Eur. J.*, 2017, **23**, 10100–10109.
40 P. Guionneau, M. Marchivie, G. Bravic, J.-F. Létard and D. Chasseau, *J. Mater. Chem.*, 2002, **12**, 2546–2551.
41 G. P. Schiemenz, *Z. Naturforsch., B: J. Chem. Sci.*, 2007, **62**, 235–243.
42 Y. Miyazaki, T. Nakamoto, S. Ikeuchi, K. Saito, A. Inaba, M. Sorai, T. Tojo, T. Atake, G. S. Matouzenko, S. Zein and S. A. Borshch, *J. Phys. Chem. B*, 2007, **111**, 12508–12517.
43 R. Kulmaczewski, L. J. Kershaw Cook, C. M. Pask, O. Cespedes and M. A. Halcrow, *Cryst. Growth Des.*, 2022, **22**, 1960–1971.
44 S. Decurtins, P. Gütlich, C. P. Köhler, H. Spiering and A. Hauser, *Chem. Phys. Lett.*, 1984, **105**, 1–4.
45 A. J. Valentine, A. M. Geer, T. J. Blundell, W. Tovey, M. J. Cliffe, E. S. Davies, S. P. Argent, W. Lewis, J. McMaster, L. J. Taylor, D. Reta and D. L. Kays, *Dalton Trans.*, 2022, **51**, 18118–18126.
46 J. Létard, P. Guionneau, O. Nguyen, J. S. Costa, S. Marcén, G. Chastanet, M. Marchivie and L. Goux-Capes, *Chem. – Eur. J.*, 2005, **11**, 4582–4589.
47 S. K. Kulshreshtha and R. M. Iyer, *Chem. Phys. Lett.*, 1984, **108**, 501–504.
48 W. Nicolazzi and A. Bousseksou, *C. R. Chim.*, 2018, **21**, 1060–1074.
49 Y. Hirai, S. Van Baaren, T. Ohmura, T. Nakanishi, T. Takeda, Y. Kitagawa, Y. Hasegawa, R. Métivier and C. Allain, *Adv. Opt. Mater.*, 2023, **11**, 2203139.
50 S.-Q. Su, S.-Q. Wu, M. L. Baker, P. Bencok, N. Azuma, Y. Miyazaki, M. Nakano, S. Kang, Y. Shiota, K. Yoshizawa, S. Kanegawa and O. Sato, *J. Am. Chem. Soc.*, 2020, **142**, 11434–11441.

This journal is © The Royal Society of Chemistry 2024

Open Access Article. Published on 22 May 2024. Downloaded on 9/16/2024 9:40:39 PM.
This article is licensed under a Creative Commons Attribution 3.0 Unported Licence.

51 E. Michaels, I. Capel Berdiell, H. B. Vasili, C. M. Pask, M. J. Howard, O. Cespedes and M. A. Halcrow, *Cryst. Growth Des.*, 2022, **22**, 6809–6817.
52 S. P. Vallone, A. N. Tantillo, A. M. dos Santos, J. J. Molaison, R. Kulmaczewski, A. Chapoy, P. Ahmadi, M. A. Halcrow and K. G. Sandeman, *Adv. Mater.*, 2019, **31**, 1807334.
53 L. Zhao, Y.-S. Meng, Q. Liu, O. Sato, Q. Shi, H. Oshio and T. Liu, *Nat. Chem.*, 2021, **13**, 698–704.
54 M. Gavara-Edo, R. Córdoba, F. J. Valverde-Muñoz, J. Herrero-Martín, J. A. Real and E. Coronado, *Adv. Mater.*, 2022, 2202551.
55 B. Kumar, A. Paul, D. J. Mondal, P. Paliwal and S. Konar, *Chem. Rec.*, 2022, **22**, e202200135.
56 M. Oppermann, F. Zinna, J. Lacour and M. Chergui, *Nat. Chem.*, 2022, **14**, 739–745.
57 Y. Jiang, L. C. Liu, H. M. Müller-Werkmeister, C. Lu, D. Zhang, R. L. Field, A. Sarracini, G. Moriena, E. Collet and R. J. D. Miller, *Angew. Chem., Int. Ed.*, 2017, **56**, 7130–7134.
58 S.-Q. Su, S.-Q. Wu, Y.-B. Huang, W.-H. Xu, K.-G. Gao, A. Okazawa, H. Okajima, A. Sakamoto, S. Kanegawa and O. Sato, *Angew. Chem., Int. Ed.*, 2022, **61**, e202208771.
59 J.-P. Xue, Y. Hu, B. Zhao, Z.-K. Liu, J. Xie, Z.-S. Yao and J. Tao, *Nat. Commun.*, 2022, **13**, 3510.
60 R. Akiyoshi and S. Hayami, *Chem. Commun.*, 2022, **58**, 8309–8321.
61 S. Johannsen, S. Ossinger, J. Grunwald, A. Herman, H. Wende, F. Tuczek, M. Gruber and R. Berndt, *Angew. Chem., Int. Ed.*, 2022, **61**, e202115892.
62 S. Johannsen, S. Schüddekopf, S. Ossinger, J. Grunwald, F. Tuczek, M. Gruber and R. Berndt, *J. Phys. Chem. C*, 2022, **126**, 7238–7244.
63 D. Li, Y. Tong, K. Bairagi, M. Kelai, Y. J. Dappe, J. Lagoute, Y. Girard, S. Rousset, V. Repain, C. Barreteau, M. Brandbyge, A. Smogunov and A. Bellec, DOI: **10.48550/ARXIV.2206.13767**.
64 S. Dehnen, *Angew. Chem., Int. Ed.*, 2018, **57**, 10386–10387.